Available online at www.sciencedirect.com
ScienceDirect
Medical Engineering & Physics 30 (2008) 91–103
Medical Engineering & Physics
www.elsevier.com/locate/medengphy

Three-phase CFD analytical modeling of blood flow

Jonghwun Jung *, Ahmed Hassanein

Mathematics and Computer Science Division, Argonne National Laboratory, 9700 S. Cass Avenue, Argonne, IL 60439, USA

Received 28 July 2006; received in revised form 20 November 2006; accepted 9 December 2006

Abstract

The behavior of blood cells in disturbed flow regions of arteries has significant relevance for understanding atherogenesis. However, their distribution with red blood cells (RBCs) and leukocytes is not so well studied and understood. Our three-phase computational fluid dynamics approach including plasma, RBCs, and leukocytes was used to numerically simulate the local hemodynamics in such a flow regime. This model has tracked the wall shear stress (WSS), phase distributions, and flow patterns for each phase in a concentrated suspension shear flow of blood. Unlike other computational approaches, this approach does not require dispersion coefficients as an input. The non-Newtonian viscosity model was applied to a wide physiological range of hematocrits, including low shear rates. The migration and segregation of blood cells in disturbed flow regions were computed, and the results compared favorably with available experimental data. The predicted higher leukocyte concentration was correlated with relatively low WSS near the stenosis having a high WSS. This behavior was attributed to flow-dependent interactions of the leukocytes with RBCs in pulsatile flow. This three-phase hemodynamic analysis may have application to vulnerable plaque formation in arteries with *in vivo* complex flow conditions.

Keywords: Three-phase flow; Wall shear stress; Non-Newtonian; Plaque formation; Hemodynamic interaction; Shear flow

1. Introduction

Atherosclerosis, a disorder of large arteries, is the result of a complex interaction of blood elements, disturbed flows, and the physiological state of the endothelium, including many pathological processes [9,30]. Several studies have suggested a correlation between atherosclerotic plaque sites, preferentially located at curvatures and branches, and hemodynamic characteristics that are induced by disturbed blood flow patterns [5,25,31,33,35].

Within the past decade, many researchers [4,8,14,26,30] have reported the migration and adhesion of leukocytes obtained from *in vitro* experiments with disturbed flows, mostly in the absence of red blood cells (RBCs), indicating that atherosclerosis-susceptible regions are strongly associated with abnormal low wall shear stress (WSS) and leukocyte–endothelium interactions in human blood flows. However, studies that ignored the RBC contributions, roughly 30–55% by volume *in vivo*, may be inadequate for extrapolating to *in vivo* conditions [27]. Because of the high cell number and particulate nature of RBCs, whole blood exhibits non-Newtonian rheology. The spatial distributions for blood elements such as plasma, RBCs, and leukocytes may vary with disturbed flows in concentrated suspensions. In such flows, aggregation of RBCs, one of the most important interparticle phenomena of blood, is a process whereby RBCs collide with one another as a result of relative motion between them and adhere to form larger RBCs. The relative motion between blood cells may be due to Brownian motion, gravity, electrical forces, flow hemodynamics, and so forth and results in dispersion of blood elements. As indicated in blood flows through capillary tubes at low shear rates [6,13,21,28], the shear-induced blood cell migration can be due to hemodynamics resulting from flow-dependent interactions between blood elements. The inward migration of RBCs was especially preferred as a result of RBC aggregation at very low shear rates. This effect might be observed because of fluid inertia and cell density differences, as indicated by Nobis et al. [28]. These hemodynamic phenomena can affect the

* Corresponding author at: Argonne National Laboratory, Mathematics and Computer Science Division, Building 308, 9700 South Cass Avenue, Argonne, IL 60439, USA. Tel.: +1 630 252 6298; fax: +1 630 252 3250.
E-mail address: jungjh@anl.gov (J. Jung).

1350-4533/$ – see front matter © 2007 Published by Elsevier Ltd on behalf of IPEM.
doi:10.1016/j.medengphy.2006.12.004

effective particle size-dependent distribution in flow of mixed suspensions of blood elements.

To investigate these complex hemodynamic characteristics of blood flow, researchers [6,24,29,34] have developed mathematical models that include a constitutive equation depending on the shear rates or the hematocrit. To compute flow hemodynamics of plasma and RBCs in large-scale vascular geometries where atherosclerosis is known to frequently occur, we suggested a multiphase non-Newtonian CFD model for the concentrated suspension flow of blood [19,20]. Most of the total hemodynamic force, WSS, was due to the RBCs but not to the plasma [19]. The model confirmed that the RBCs determine the rheological behavior of blood, a result impossible to prove with the single-phase CFD model. The relation between hemodynamic forces and the distribution of blood elements can be considered an important factor for the progression of atherosclerosis. Vulnerable plaques, in particular, tend to coincide with locations at which hemodynamic stresses acting on plaques due to flow obstruction are concentrated [9]. Hence, it would be more useful to consider whole blood as three-phase: a nonhomogeneous fluid consisting of RBCs and leukocytes suspended in plasma.

In this study, the multiphase model is extended to include the blood rheological properties at low shear rates with leukocytes. This study presents a novel numerical simulation of leukocyte migration due to flow-dependent interactions with RBCs in disturbed flow regions. We address the hypothesis that the leukocytes' adhesion to the vascular wall is determined, in part, by the relation between hemodynamic stresses and inhomogeneities resulting from the migration of blood elements in suspension flows.

2. Methods

2.1. Flow systems

To test the underlying hypothesis of local hemodynamics regarding the distribution and migration of blood elements, we used a 3D *in vitro* tubular flow system with a sudden expansion geometry reported by Karino and Goldsmith [21], where some experimental results are available (Fig. 1a). Two experimental cases in steady flow with the constant inlet velocity (U_i) were investigated—case 1: the dilute flow for the

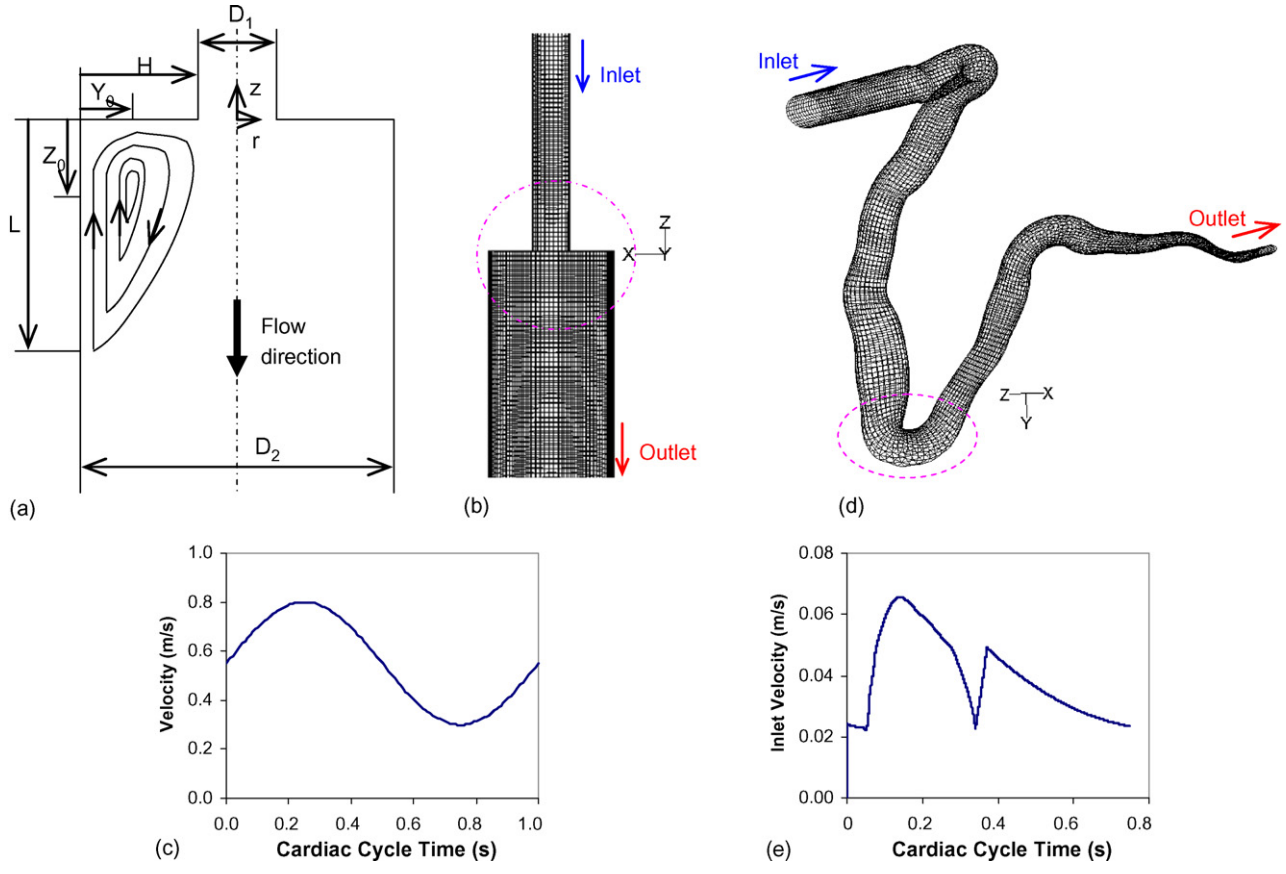

Fig. 1. (a) Schematic diagram of 3D tubular flow system with sudden expansion geometry for studying cases 1–3 [21], (b) 3D computational mesh generated using a Cooper volume-meshing scheme based on hex elements and the GAMBIT software, and (c) pulsatile inlet velocity profile for 3D tubular flow. The circle in (b) shows an idealized model, like the stenosis area in a vessel. The upstream tube diameter (D_1) = 151 μm, the downstream tube diameter (D_2) = 504 μm, and the step height (H) = 1/2($D_2 - D_1$). L: the reattachment point, Z_0: the axial distance to the vortex center, and Y_0: the radial distance to the vortex center. (d) 3D computational mesh of realistic RCA for studying case 4 adapted from Refs. [2,20], and (e) pulsatile inlet velocity profile for RCA [20]. The circle in (d) shows a maximum curvature of tortuous reduction in the area. The inlet area = 15 mm^2, the outlet area = 2.2 mm^2.

motion of hardened human red cells suspended in water, and case 2: the concentrated flow of RBCs suspended in plasma. The computational mesh (Fig. 1b) for flow system was generated by using the GAMBIT software (from Fluent Inc.) and then adapted for the multiphase 3D simulations.

To study the distribution of blood elements due to flow-dependent interaction with RBCs, we simulated two three-phase cases of pulsatile flow (Fig. 1c and e) including leukocytes—case 3: the concentrated flow in the case 2 system, and case 4: the concentrated flow in a long segment of realistic right coronary artery (RCA) used in previous work [2,20]. In the simulation, we used a 3D computational mesh of RCA without side branches (Fig. 1d). Of specific interest was the dispersion of blood elements in the disturbed flow regions of the sudden expansion and/or the curvature geometries, such as stenosis in a vessel, indicated by circles.

2.2. Multiphase CFD model

In the non-Newtonian 3D CFD model, which treats blood as an inhomogeneous fluid, a suspension is a multiphase system wherein two dispersed phases consisting of RBCs and leukocytes are suspended in plasma. We have adopted the multiphase CFD approach proposed in Gidaspow [12] and Anderson and Jackson [1] for describing the hemodynamics of blood flows, since this approach can excellently describe the hemodynamics of the system of interest comprising a large number of closely spaced RBCs, which have a hematocrit or volume fraction range of roughly 30–55% *in vivo* [19,20]. The concept of local mean variables was used to translate the Navier–Stokes equations for the fluid and the Newtonian equations of motion for the particles directly into coupled continuum equations representing momentum balances. Compared with a single-phase model, the multiphase model includes the volume fraction for each phase, as well as mechanisms for the exchange of momentum, heat, and mass between the phases.

2.2.1. Continuity equations

The continuity equation for each phase (k = plasma, RBCs, leukocyte) is given by

$$\frac{\partial(\rho_k \varepsilon_k)}{\partial t} + \nabla \cdot (\rho_k \varepsilon_k \vec{v}_k) = 0, \tag{1}$$

where ρ is the density, ε the volume fraction, t the time, and v is the velocity. In addition, the volume fraction of each phase must sum to one as

$$\sum_{k=1}^{\mathrm{np}} \varepsilon_k = 1.0, \tag{2}$$

where np is 3, the total number of phases. The volume fraction occupied by one phase cannot be occupied by other phases. The blood mixture density, ρ_{mix}, is given by the sum of the volume-fraction-weighted densities for the plasma, RBCs, and leukocytes without considering other minor blood constituents:

$$\rho_{\mathrm{mix}} = \varepsilon_{\mathrm{plasma}}\rho_{\mathrm{plasma}} + \varepsilon_{\mathrm{RBC}}\rho_{\mathrm{RBC}} + \varepsilon_{\mathrm{leukocyte}}\rho_{\mathrm{leukocyte}}. \tag{3}$$

2.2.2. Momentum equations

The momentum equation for each phase (k = plasma, RBCs, leukocyte) is given by

$$\frac{\partial(\rho_k \varepsilon_k \vec{v}_k)}{\partial t} + \nabla \cdot (\rho_k \varepsilon_k \vec{v}_k \vec{v}_k) = -\varepsilon_k \nabla p + \nabla \cdot \bar{\bar{\tau}}_k + \varepsilon_k \rho_k \vec{g} + \sum_{\substack{l=l,m,n \\ l \neq k}} \beta_{kl}(\vec{v}_l - \vec{v}_k) + \vec{F}_k, \tag{4}$$

where p is the pressure, τ the stress tensor, g the gravity force, and F is the external forces such as virtual mass, rotational and shear lift, electricity, and magnetism. In the drag force, β_{kl} represents the interphase momentum exchange coefficients for plasma and RBCs, plasma and leukocytes, and RBCs and leukocytes. In order to solve the conservation equations (Eqs. (1) and (4)), the appropriate modified constitutive relations such as the particle–particle interaction (stress terms) and fluid–particle interaction (drag and external force terms) must be determined for blood flows.

2.3. Constitutive equations

2.3.1. Plasma stress tensor

The stress tensor for the plasma phase is given by the Newtonian form:

$$\bar{\bar{\tau}} = \varepsilon\mu(\nabla\vec{v} + (\nabla\vec{v})^{\mathrm{T}}) + \varepsilon\left(\kappa - \frac{2}{3}\mu\right)\nabla \cdot \vec{v}\bar{\bar{I}}. \tag{5}$$

here ε, κ, and μ are volume fraction, bulk viscosity (which is assumed to be zero), and shear viscosity for the plasma phase, respectively, and I is a unit tensor. The plasma viscosity, μ_{plasma} is treated as a Newtonian fluid having a constant viscosity.

2.3.2. RBC stress tensor

The stress tensor for the RBCs phase, the particle–particle interaction, is given by

$$\bar{\bar{\tau}} = -p\delta + \varepsilon\mu(\nabla\vec{v} + (\nabla\vec{v})^{\mathrm{T}}) + \varepsilon\left(\kappa - \frac{2}{3}\mu\right)\nabla \cdot \vec{v}\bar{\bar{I}}, \tag{6}$$

where δ is the Kronecker delta. The pressure, p_{RBC}, arises as a result of the collision of the particles and represents an interparticle pressure as a function of volume fraction of RBCs, i.e., $\varepsilon_{\mathrm{RBC}}$. The κ and μ represent effective bulk and shear viscosities for the RBCs assembly, depending on the volume fraction of RBCs and the shear rate.

In the simulation, the interparticle pressure for a suitable hematocrit range was negligibly small [20] because blood behaves like a fluid even at 98% hematocrit by volume [11]. The κ_{RBC} was assumed to be zero. The behavior of RBCs in

shear flow was represented by the product of effective viscosity and the deformation tensor of the cell. A modification of the Carreau–Yasuda viscosity model was used to describe the non-Newtonian shear-thinning rheological behavior of blood flow. Hence, the effective RBC shear viscosity, μ_{RBC}, was calculated from the equation for dimensionless relative blood mixture viscosity, η, in a non-Newtonian shear thinning fluid:

$$\eta = \frac{\varepsilon_{RBC}\mu_{RBC} + \varepsilon_{plasma}\mu_{plasma} + \varepsilon_{leukocyte}\mu_{leukocyte}}{\mu_{plasma}} = m[1 + (\lambda\dot{\gamma})^2]^{(n-1)/2}, \quad (7)$$

where m, λ, and n are parameters defined below, and $\dot{\gamma} = (\nabla\vec{v} + (\nabla\vec{v})^T)$ is the shear rate ($1/s$). The dimensionless shear rate ($\bar{\dot{\gamma}}$) is given by $1 + (\lambda\dot{\gamma})^2$.

Fig. 2 shows an empirical relation for low shear rates. The time constant, λ, was taken to be 0.110 s and the two parameters n and m as a function of the hematocrit, $H = \varepsilon_{RBC}$, were given by the following polynomial approximations for

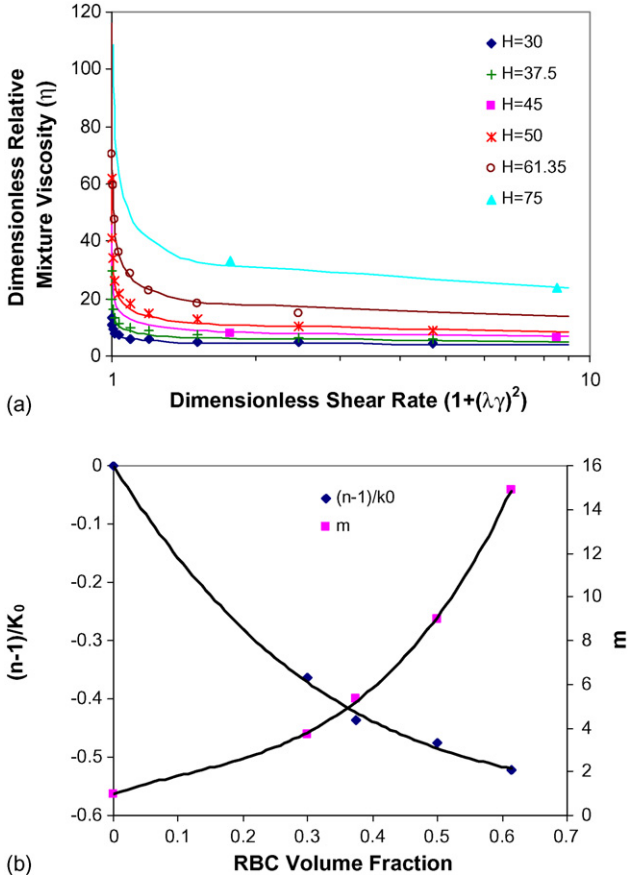

Fig. 2. (a) Dimensionless relative blood viscosity (η), as function of dimensionless shear rate ($1 + (\lambda\dot{\gamma})^2$) and hematocrit ($H$), obtained from experimental data for blood [3,38]. (b) Parameters m and n were determined as a function of RBC volume fraction at low shear rates ($1 + (\lambda\gamma)^2 \leq 1.5$). The points represent the experimental data at the different hematocrits and shear rates.

$\bar{\dot{\gamma}}$ greater than 1.5 ($\dot{\gamma} \geq 6$) [19]:

$$n = 0.8092\varepsilon_{RBC}^3 - 0.8246\varepsilon_{RBC}^2 - 0.3503\varepsilon_{RBC} + 1,$$
$$m = 122.28\varepsilon_{RBC}^3 - 51.213\varepsilon_{RBC}^2 + 16.305\varepsilon_{RBC} + 1 \quad (8)$$

For $\bar{\dot{\gamma}}$ less than 1.5 ($\dot{\gamma} \leq 6$) at low shear rates (also see Fig. 2), these were as follows:

$$\frac{n-1}{k_0} = -0.8913\varepsilon_{RBC}^3 + 2.0679\varepsilon_{RBC}^2 - 1.7814\varepsilon_{RBC},$$
$$m = 70.782\varepsilon_{RBC}^3 - 22.454\varepsilon_{RBC}^2 + 9.7193\varepsilon_{RBC} + 1 \quad (9)$$

Here, $k_0 = \ln(\ln\bar{\dot{\gamma}})/\ln\bar{\dot{\gamma}}$.

This model was applied to a wide physiological range of hematocrits and the shear rate compared with the experimental data [3,38]. The model included the effect of RBC agglomeration, which is described by the increase of the effective RBC viscosity at low shear rates [11], as a function of the volume fraction of RBCs and the shear rate. In the case of two-phase flow, the leukocyte term was dropped from Eq. (7).

2.3.3. Leukocyte stress tensor

The stress tensor for the leukocyte phase, the particle–particle interaction, is given by

$$\bar{\bar{\tau}} = -p\delta + \varepsilon\mu(\nabla\vec{v} + (\nabla\vec{v})^T) + \varepsilon\left(\kappa - \frac{2}{3}\mu\right)\nabla\cdot\vec{v}\bar{\bar{I}}, \quad (10)$$

where p, ε, κ, and μ are interparticle pressure, volume fraction, bulk viscosity, and shear viscosities for the leukocyte phase, respectively.

In the simulation, the $p_{leukocyte}$ was assumed to be zero, because of a low volume fraction less than 1%. The κ_{RBC} was also assumed to be zero, and the μ_{plasma} was treated as 7.5cP times the leukocyte volume fraction.

2.3.4. External forces

As a particle moves through a viscous fluid, a resistance to its motion is caused by the interphase drag. The fluid–particle interaction, that is, the plasma–blood cell interaction, was described by the interphase momentum exchange coefficients, β, and velocity differences between the continuous phase (cp) and dispersed phase (dp). The coefficients are Schiller and Naumann model used in our previous work [19,20]:

$$\beta = \frac{3}{4}C_d\frac{\rho_{cp}\varepsilon_{cp}\varepsilon_{dp}\left|\vec{v}_{cp} - \vec{v}_{dp}\right|}{d_{dp}\phi}, \quad (11)$$

where the drag coefficient, C_d, on a single sphere is related to the Reynolds number, Re_p, as follows:

$$C_d = \frac{24}{Re_p}[1 + 0.15\,Re_p^{0.687}] \quad \text{for } Re_p < 1000 \quad (12)$$

$$C_d = 0.44 \quad \text{for } Re_p \geq 1000 \tag{13}$$

$$Re_p = \frac{\rho_{cp} d_{dp} \left|\vec{v}_{cp} - \vec{v}_{dp}\right| \phi}{\mu_{cp}}, \tag{14}$$

where d is the diameter of blood cells and ϕ is the dynamic shape factor. More drag is experienced by the agglomerate nonspherical particles in fluid [16]. The dynamic shape factor of RBCs was used to describe the effect of RBC agglomeration for $\bar{\dot{\gamma}}$ less than 1000 ($\dot{\gamma} \leq 300$):

$$\phi = 1.5\bar{\dot{\gamma}}^{-0.058697} \tag{15}$$

Except for the shape factor of RBCs in $\bar{\dot{\gamma}}$ less than 1000, the shape factor of RBCs and leukocytes for computing the drag force was assumed to be spherical without the agglomeration, that is, $\phi = 1$. For β between a RBC and leukocyte, the Reynolds number is given by

$$Re_p = \frac{\varepsilon_{RBC}\rho_{RBC} d_{leukocyte} \left|\vec{v}_{RBC} - \vec{v}_{leukocyte}\right| \phi}{\varepsilon_{RBC}\mu_{RBC} + \varepsilon_{leukocyte}\mu_{leukocyte}} \tag{16}$$

The coupling between the momentum equation (Eq. (4)) for the three phases is made explicitly by six drag terms. The sum of the drag forces for Eq. (4) is zero [12].

Two external forces of virtual mass and shear lift forces for the fluid–particle interaction were relatively small compared with the drag forces [20]. In this simulation, we adopted both models that were used in our previous work [20]. Other external forces such as electrical force were neglected.

2.4. Numerical approach

To obtain the numerical solution of nonlinear-coupled partial differential equations given above with appropriate initial and boundary conditions, we used the commercial code FLUENT 6.1 [10], which uses a multiphase 3D Eulerian–Eulerian model. The numerical solution method uses an implicit, finite-volume, unstructured mesh, staggered grid arrangement. A volume fraction correction equation in the continuity equations was used for the numerical convergence. The maximum residual was 10^{-3} for flow systems on a personal computer with 3.2 GHz processor. The mass flux at the inlet

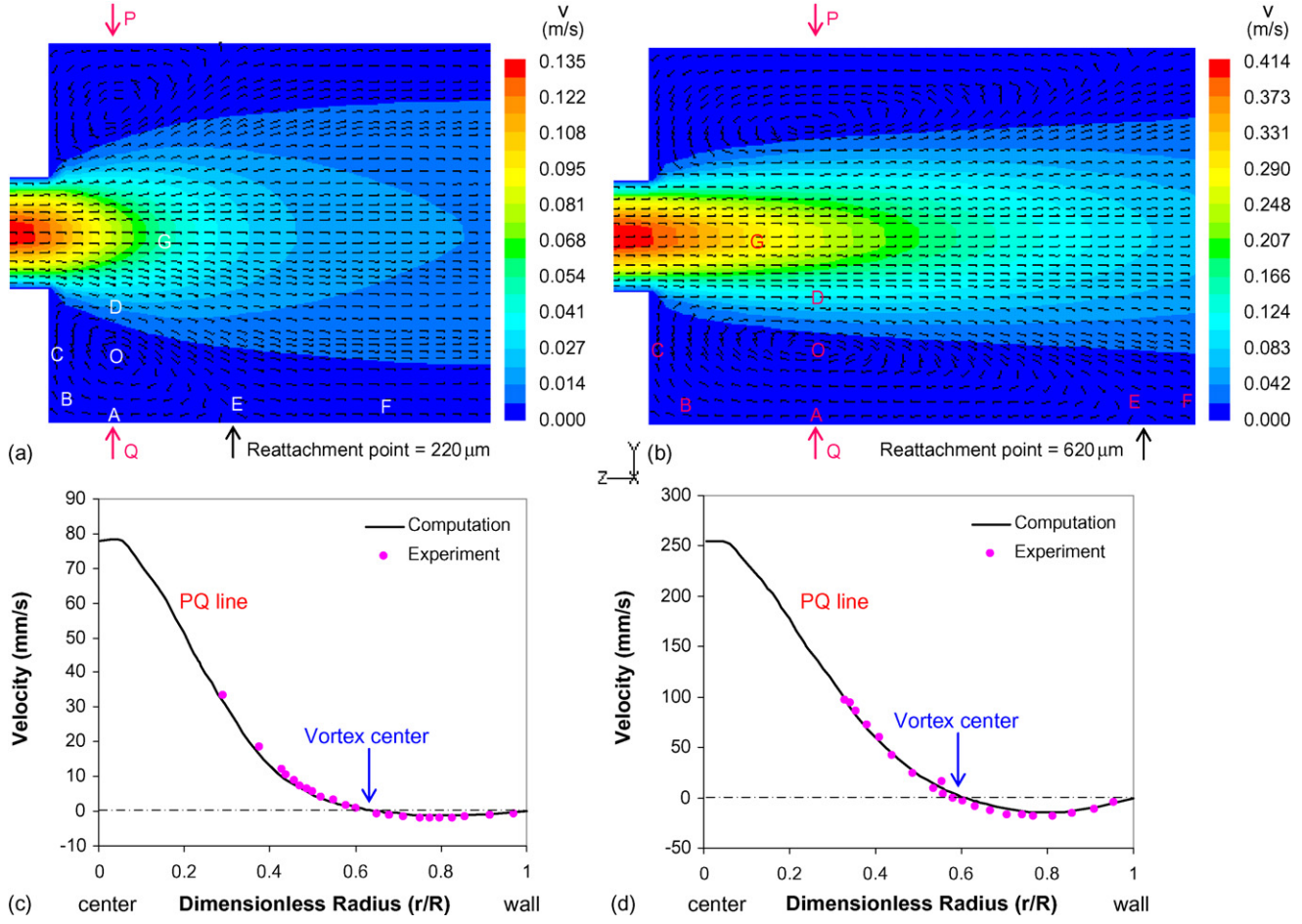

Fig. 3. Comparison of the computed velocity and the measured velocity [21] for 1% hardened human red cells ($d_p = 7.5$ μm, $\rho = 1.13$ g/cm^3) by volume suspended in water ($\rho = 1.0$ g/cm^3, $\mu = 0.01$ P) in the case 1: (a) velocity contours for $Re = 12.2$ and $U_i = 7.57$ cm/s, (b) velocity contours for $Re = 37.8$ and $U_i = 23.3$ cm/s, (c) velocity for PQ line through vortex center of (a), and (d) velocity for PQ line through vortex center of (b). Reynolds number ($Re = \rho_{mix} U_{mean} D_1/\mu_{mix}$) is based on the upstream tube diameter (D_1) and the upstream mean velocity (U_{mean}).

and the outlet was matched within the range of 10^{-9} for all simulation cases.

Multiphase CFD models generally have been validated by comparing calculated results with the measured data for spatial and temporal velocities and concentrations obtained from experimental techniques [12,18,22]. The current CFD models with the non-Newtonian shear-thinning model were initially validated for a neutrally buoyant dense suspension flow and the application of blood flows [19]. Computational results compared favorably with available experimental data in cases 1 and 2.

The boundary conditions for zero slip velocity at rigid walls were employed for each phase in the simulations. For initial conditions, the velocities were set to zero. More specified physics models of the non-Newtonian shear-thinning viscosity, the transient inlet-mixture velocity waveforms, the lift force, and the drag force were programmed into the FLUENT code as individual subroutines. All simulations were carried out in the 3D computational domain.

3. Results

We applied our multiphase CFD model including the constitutive relations in order to estimate the hemodynamics and distributions of blood elements in disturbed flow regions. As expected, the two-phase dilute flow simulation (case 1) of hardened human red cells in steady-state condition agreed well with experimental results [21] in the vortex formations, reattachment points, and velocity profiles (Fig. 3). The velocities on the PQ line of the cross section through the vortex center showed the best match to the measured veloc-

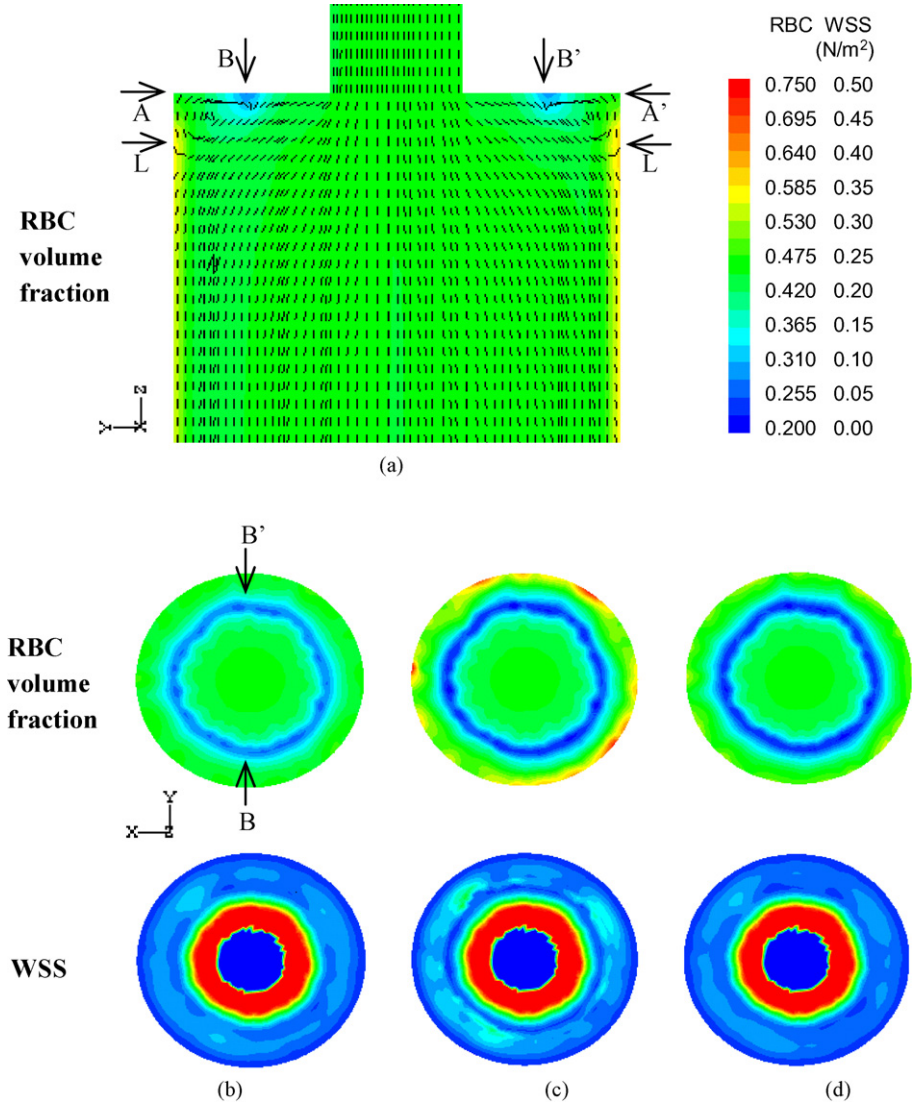

Fig. 4. Comparison of driving forces (Eqs. (9) and (15)) determining the distribution of 45% RBCs ($d_p = 8.2\,\mu m$, $\rho = 1.10\,g/cm^3$) by volume suspended in plasma ($\rho = 1.02\,g/cm^3$, $\mu = 0.02\,P$) of the case 2 ($U_i = 11\,cm/s$). Computational simulations (a) and (b) without Eqs. (9) and (15), (c) with only Eq. (9), and (d) with both Eqs. (9) and (15) for the effect of RBC agglomeration at low shear rates. The cross sections of (b)–(d) were obtained from the A–A′ slice indicated in (a). The color indicates the RBC volume fraction and WSS. The direction for gravity is negative *Z*.

Table 1
Comparison of computational (Fig. 3a and b) and experimental [21] particle velocity magnitude (mm/s) in vortex regions

Location	$Re = 12.2$		$Re = 37.8$	
	Experiment	Computation	Experiment	Computation
O	0.54	0.92	2.44	5.17
A	0.64	0.36	3.59	3.88
B	0.36	0.26	3.03	1.41
C	1.46	0.82	6.93	4.05
D	11.8	13.7	94.1	92.1
E	0.3	0.27	0.84	1.29
F	3.3	2.61	0.95	3.73
G	48.6	50.97	272	283

ities. The velocities at all points indicated in Fig. 3a and b agreed within the same order of magnitude, as shown in Table 1.

We also studied two-phase concentrated flow behavior (case 2) with 45% RBCs suspended in plasma. Two terms, Eqs. (9) and (15), added to determine driving force at low shear rates, were estimated at the same condition (Fig. 4), where the inlet velocity (U_i) was 11 cm/s. The primary vortices formed close to the wall of A–A′ slice. There were also tiny secondary vortices (points B and B′) with relative lower RBC volume fraction. The secondary ones moved inward along the wall of the A–A′ slice with the decrease of inlet velocity (U_i). The relative higher RBC volume fraction occurred around the reattachment regions (L) of the downstream tube wall, as also predicted in dilute flow (Fig. 3) and found in the *in vitro* experimental results [8,30]. The thin layer of the relative higher plasma volume fraction (red cell poor-plasma region) was predicted near the wall of the upstream

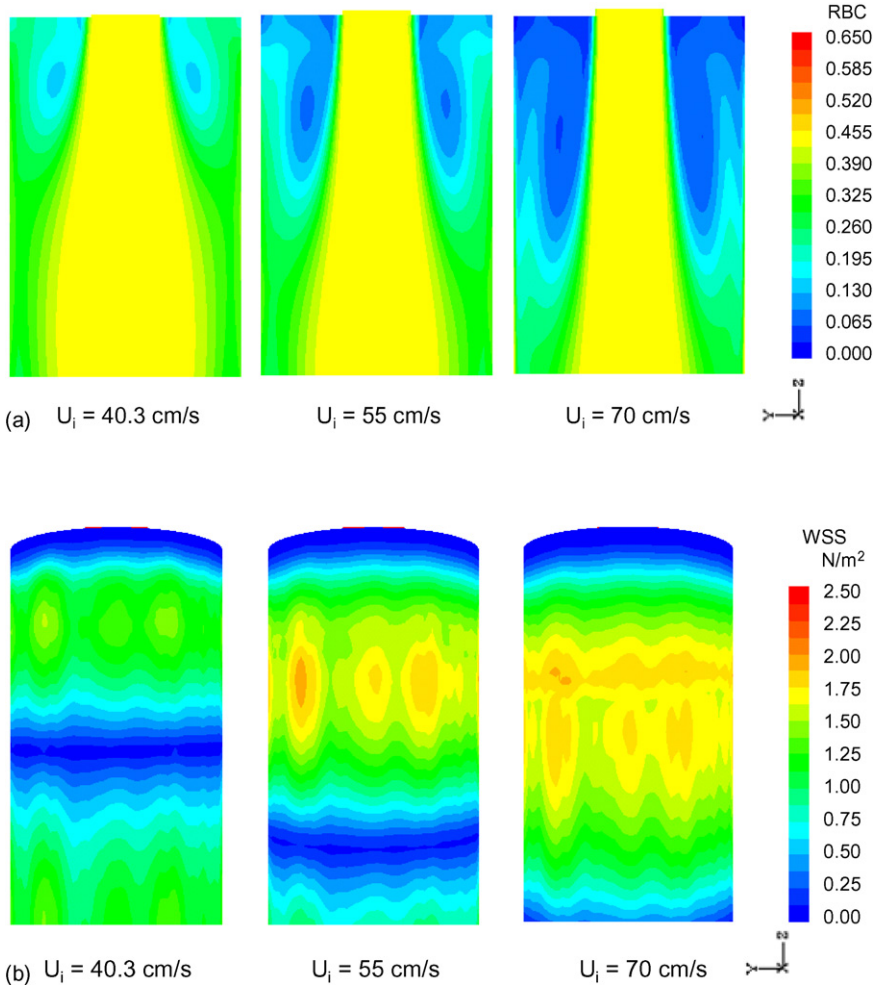

Fig. 5. Computed (a) RBC volume fraction and (b) WSS with the increased inlet velocities in case 2.

tube, as observed in experiments of blood flow through small vertical tubes [6].

With the non-Newtonian viscosity model (Eq. (7)) having the parameters of Eq. (9) at low shear rates (Fig. 4c), the RBC volume fraction in the secondary vortex region forming a ring type on the wall of A–A′ slice decreased from 0.27 to 0.2. The RBC volume fraction in the edge of the slice, on the other hand, increased to 0.75 and then decreased to near the 0.45 by adding the effect of the shape factor (Eq. (15)) for drag forces (Fig. 4d). The WSS of Fig. 4c slightly decreased in the region of the secondary vortex when compared with other cases (Fig. 4b and d).

We also estimated the effect of the inlet velocity (U_i) in the CFD model including both Eqs. (7) and (15) (Fig. 5). With the increase of the inlet velocity (U_i), the secondary vortex moved outward along the wall of the A–A′ slice and then stayed at the corner between the edge of the slice and the wall of the downstream tube. The lower RBC volume fraction was computed in this corner. The computed dimensionless reattachment distance indicated by L/H linearly increased as a function of the inlet velocity (Fig. 6a), in agreement with experimental results [21] within 8% error of the multiphase CFD computation, which is more accurate than the single-phase CFD computation.

The predicted phenomena on the distribution of RBC volume fraction as a function of the inlet velocity (Fig. 5a) showed a trend similar to the behavior captured by photomicrographs in experiments [21], in which RBCs were observed to migrate out of the vortex. The WSS was lower in the reattachment regions and at the corner of the expansion enclosed by the larger primary annular vortex and the wall (Fig. 5b). The dimensionless axial distance to the vortex center (Z_0/H) linearly increased as a function of the inlet velocity (Fig. 6b). The dimensionless radial distance to the vortex center (Y_0/H) converged to 0.57 as a function of the inlet velocity (Fig. 6b). Both distances were calculated from the multiphase CFD computation.

The migration behavior of blood cell in the vortex of the disturbed flow regions was estimated from hemodynamics (Fig. 7) obtained from the PQ line through the vortex center, as shown in Fig. 3. The velocity distributions showed a parabolic profile with 45% RBCs by volume in the core region of expansion. On the other hand, they showed a circulating flow with the vortex formation due to reverse flow in the annular region of expansion, in which low velocity (i.e., low shear rate) exists with high RBC viscosity. In the case of 0.24 cm/s, RBC viscosity in the vortex region increased when compared with other inlet velocities as a result of the effect of Eqs. (9) and (15) at the low shear rate and the high RBC volume fraction. The RBC volume fraction was depleted in the vortex center of the annular region.

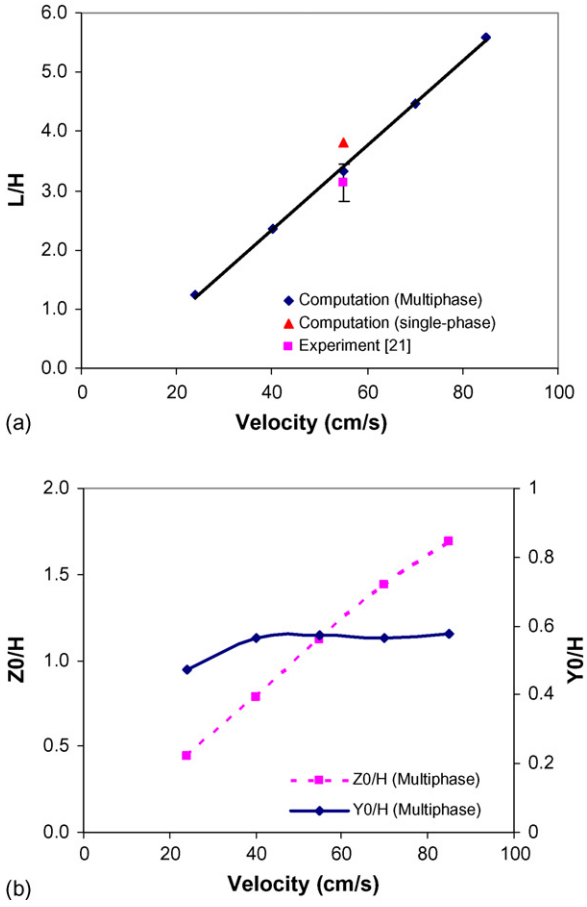

Fig. 6. Comparison of (a) the reattachment point (L) and (b) axial and radial distance to the vortex center in steady-state flow as a function of inlet velocity (U_i) in case 2.

Three-phase concentrated flow behavior of blood (case 3) including 0.5% leukocytes by volume was studied at the same configuration with a pulsatile inlet velocity profile (Fig. 8). The inlet velocity was a sine function periodic with a cardiac cycle time (t_0) of 1 s and an average velocity of 55 cm/s (Fig. 1c). The segregation of blood elements was described

Table 2
Comparison of hemodynamic values averaged for a cardiac cycle (0.735 s) in the points of Fig. 10

	Point 1	Point 2	Point 3-1	Point 3-2	Point 4
WSS[a] (N/m^2)	**2.82**	1.98	1.21	0.55	0.67
RBC[b] (%)	17.33	**23.11**	22.67	11.78	−1.11
Leukocyte[b] (%)	−2.60	5.40	**7.20**	3.60	2.80
Viscosity[a] (Kg/m-s)	0.0039	0.0047	0.0059	**0.0064**	0.0041

Bold values signify maximum hemodynamic value.

[a] Total mixture value is volume-fraction-averaged value.

[b] % value = $((A - A_0)/A_0) \times 100$, A: hemodynamic value; A_0: initial hemodynamic value; A_0 for RBC: 0.45; A_0 for leukocyte: 0.005.

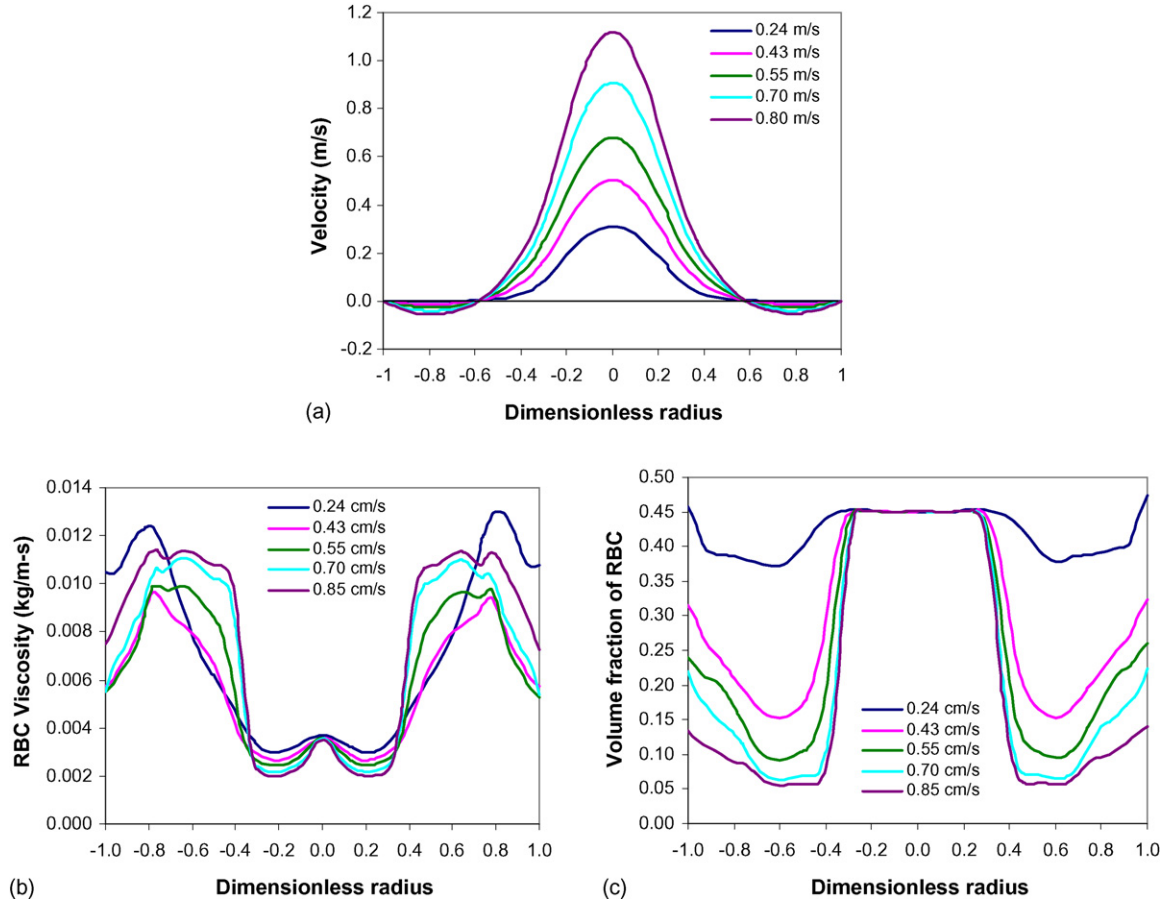

Fig. 7. Hemodynamic factors obtained from the PQ line through vortex center, as shown in Fig. 3, with the different inlet velocities (U_i) in case 2. The PQ line varied with the inlet velocity.

as their distribution indicated by volume fraction averaged for a 1 s period. The leukocytes were trapped in the vortex regions, especially in the tiny secondary vortex, in which a lower RBC concentration was computed, as observed also by experiments [21].

Similar calculations were done for a realistic human RCA with nonuniform geometry varied along the length (case 4). The inlet velocity was a pulsatile flow with the cardiac cycle period of 0.735 s, as described in Jung et al. [20] and shown in Fig. 1e. A quasi-steady-state condition was established after a

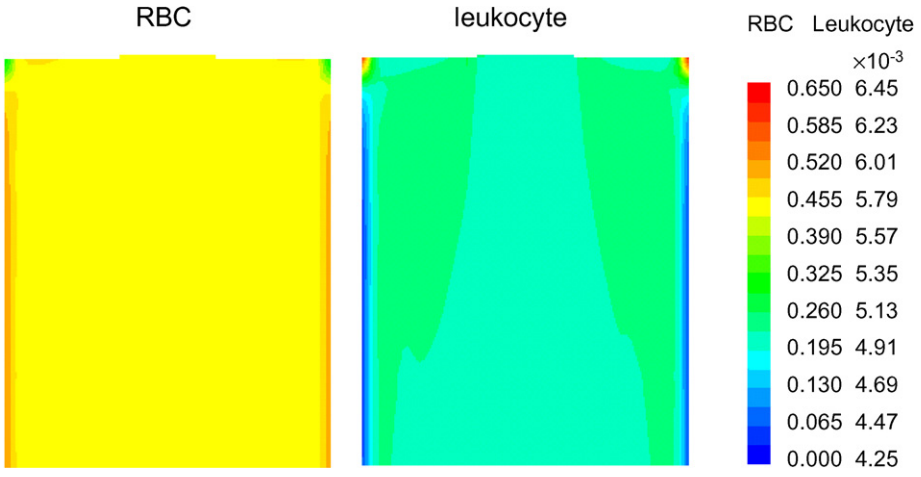

Fig. 8. Comparison of distributions of blood elements predicted from the three-phase CFD simulation consisting of 54.5% plasma, 45% RBCs, and 0.5% leukocytes ($d_p = 18\,\mu m$, $\rho = 1.064\,g/cm^3$) by initial volume of case 3. The color indicates the volume fractions of RBCs and leukocytes. The values were averaged for $t = 1$ s, where the inlet velocity of the sine function is periodic with period $2\pi t/t_0$ ($t_0 = 1$ s) and magnitude of 25 cm/s.

cardiac cycle time of 14 s (Fig. 9). This state occurred because of the limit cycle behavior of slowly established leukocyte buildup. The maximum curvature having a tortuous reduction area (Fig. 10), like stenosis, was compared with the sudden expansion geometry in the 3D *in vitro* tubular flow system described in cases 2 and 3. Typical leukocyte concentration and WSS versus cardiac cycle time at the two points in Fig. 10 are presented (Fig. 11). The hemodynamic values averaged for a cardiac period of 0.735 s are given in Table 2. High WSS and the lowest leukocyte volume fraction were predicted at the reduction area of the maximum curvature on the inside RCA curvature, namely, the stenosis region. Depending on the distance from this region to the upstream and downstream regions, the middle WSS corresponded with the highest RBC and leukocyte volume fractions. Relatively low WSS correlated with high leukocyte volume fraction was predicted downstream and upstream of this curvature, in which leukocyte segregation due to RBCs interactions was observed. High leukocyte depositions were generally predicted at the reverse pressure gradient over the flow direction. High viscos-

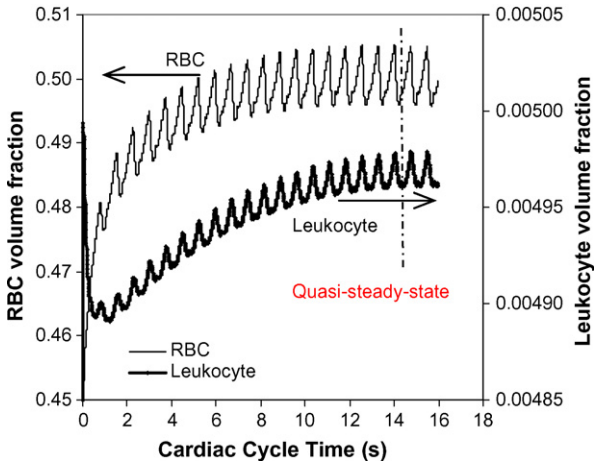

Fig. 9. Quasi-steady state conditions for the three-phase simulation in the realistic RCA (case 4). RBC and leukocyte volume fraction were obtained at a point of maximum curvature indicated in Fig. 1d.

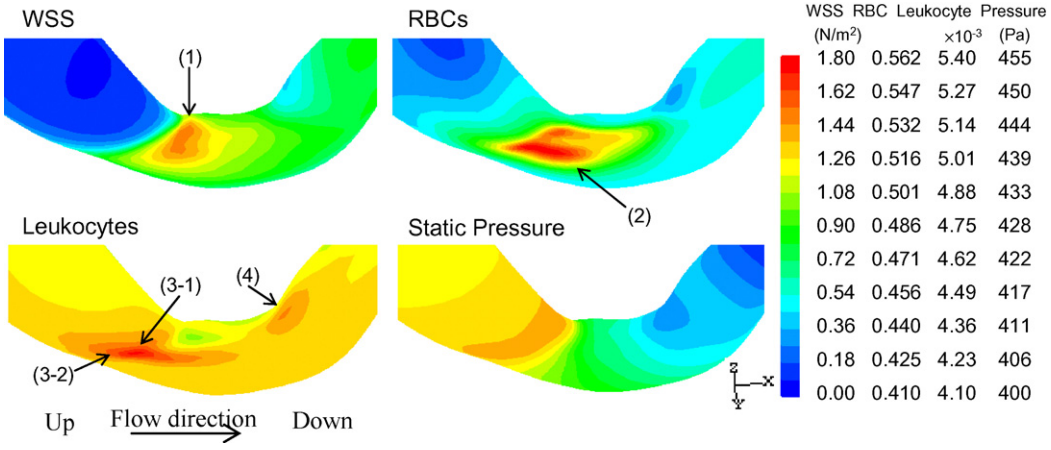

Fig. 10. Snap shot of hemodynamic factors at the diastole in the maximum curvature of the RCA [20] indicated by a circle (Fig. 1d): (1) point with highest WSS, (2) point of maximum RBC buildup, (3-1) point of upstream and maximum leukocyte buildup, (3-2) point of upstream, and (4) point of downstream.

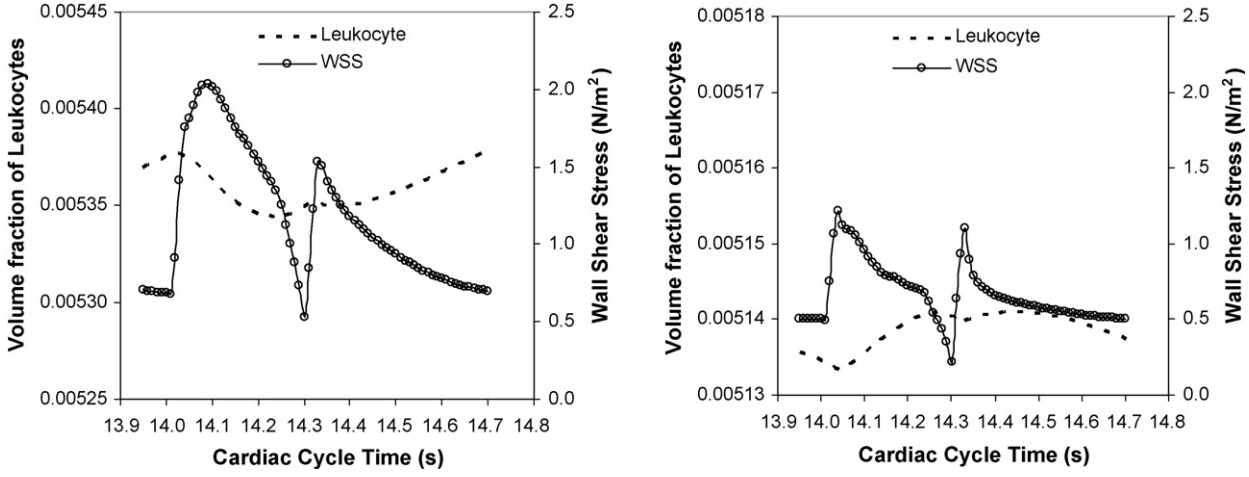

Fig. 11. Temporal variations of the leukocyte and the WSS upstream (3-1) and downstream (4) indicated in Fig. 10.

ity was also predicted upstream, where RBC and leukocyte concentrations are higher than those downstream.

4. Discussion and conclusions

A critical review of the biomedical literature shows that single-phase CFD models, which treat blood as a homogeneous fluid, cannot provide the information on hemodynamic factors needed to quantify the interactive effects and the spatial distribution of particulate matter. In the computational modeling including blood cells, the interactions between RBCs and leukocytes were analyzed by using a 2D lattice Boltzmann approach in a capillary tube [34]. RBC deformation and hydrodynamic interactions were investigated by using adaptive computational meshes in intermediate-sized microvessels [7]. However, those approaches for modeling individual particle motion are limited to simple geometry and few blood cell counts. Because of the significant amount of computing time required, they are not currently applicable to large-scale vascular geometries of the flow comprising a considerable number of closely spaced blood cells [24].

A particle trajectory model considering particle–wall interactions was suggested for large-scale vascular geometries, as an image-based CFD model [24]. For dilute flow, the dominant forces proved to be the drag and pressure gradient terms; other contributions were negligible. The model indicated the probability of blood particle deposition in femoral bypass graft anastomosis. However, the model was limited to dilute flow of a relatively small number of cells (less than 50,000 particles) compared with whole blood cells (10^9 cells/ml for RBC). The influence of RBCs on the monocyte trajectories was treated by a dispersion coefficient. In this case, the effect of RBC interactions could not be correctly estimated for whole blood of the concentrated suspension shear flow.

An image-based multiphase non-Newtonian CFD model including RBCs was suggested to test the underlying hypotheses of local hemodynamics for blood flow using the concept of local mean variables [19,20]. This approach does not require dispersion coefficients as an input. Local volume fraction and flow patterns for each blood elements were computed. The dominant driving forces proved to be the particle–particle interaction and the fluid–particle interaction, especially drag terms [20]. Two terms, Eqs. (9) and (15), added in both driving forces were used to describe the distribution of blood elements resulting from RBC agglomeration at low shear rates (Fig. 4). The added shape factor is similar to a correction to the drag due to the presence of other particles in fluid [12]. This factor controls high packing of blood cells at low shear rates, which may cause divergence in the numerical simulation, as shown in the effect due to interparticle pressure or the radial distribution function.

In a comparison of the dilute flow and the concentrated flow including only one particle size (Figs. 3 and 5), the behavior of blood cells showed similar hemodynamic trends in vortex formation, deposition of blood cells to the reattachment wall region, and WSS in disturbed flow regions, except for exact positions and numerical values. In the dilute flow, the trends were computed from the particle trajectory model [15,23] and the multiphase model [17] for large-scale systems, as observed in 3D *in vivo* tubular experiments [14].

When including two different particle sizes of RBCs and leukocytes suspended in plasma, the distribution of blood cells can be varied because of the driving forces between phases in pulsatile flow. In contrast to the behavior of cells of single particle size, leukocytes that are of larger particle size in nonhomogeneous blood flow moved to the tiny secondary vortex depending on the geometry and inlet velocity, resulting in a computed high volume fraction of leukocytes (Fig. 8). The distributions predicted in this study, compared to the behavior of RBC aggregates or latex spheres larger than a single RBC in diameter, remained within the vortex, as observed in the expansion flow [21].

Application of three-phase hemodynamic analysis to a realistic RCA (Fig. 10) predicted the relation between geometry and flow hemodynamics, even in the absence of a model for biochemical interactions between blood cells and vascular surface. The distributions (segregation) of blood elements, WSS, and pressure in such complex helical flows with multiple 3D curvatures can be due to the differences in blood cell size and density, interactions between blood cells, and inlet velocity of pulsatile flow. The transitional behavior of RBC and leukocyte depending on the WSS were calculated (Fig. 10 and Table 2). Relatively low WSS with high leukocyte volume fraction occur downstream and upstream of the maximum curvature, while the highest WSS was found at plaque location with lowest leukocyte volume fraction. Leukocyte concentration was varied by RBC dispersion and WSS distribution in such a region. The disturbed flow was calculated near the curvature with tortuous reduction area [20], similar to those shown in Figs. 5–7. The scientific literature [25,35,36] indicates that the endothelium is more easily penetrated by the leukocytes and proteins with the prolonged residence time due to vortex formation in the flow separation region. The relationship between shear stress and phase distribution is an important determinant of regional atherosclerosis and subsequent plaque progression, whereas high tensile stress (pressure/area) upstream near the highest WSS (Fig. 10, point 1) is the major determinant of plaque rupture. The results of our study provide a mechanistic insight into the behavior of different blood particles with WSS and tend to support recent clinical conclusions [9,33,37] regarding the progress of atherosclerosis. Considering minor obstruction on the curvature of artery, this multiphase model offers great promise in helping scientists understand how current hemodynamic environments lead to the creation of a new hemodynamic environment that, in turn, leads to the progression of rupture-prone vulnerable plaque. With cardiovascular imaging tests such as intravascular ultrasonography, computed tomography, and magnetic resonance imaging used to detect the composition of atherosclerotic plaque [32], this

computational technique may become an important tool to advance our knowledge of intravascular hemodynamics in artery disease development and progression.

Before this computational technique is directly applied to human RCA with tapering and bifurcations, further clinical, experimental, and computational work will be necessary to test the suggested hypothesis. The limitations of this computational approach include the exclusion of the deformability and variations in shape of blood constituents that can affect particle–particle interactions. Wall motion and electrical force may affect blood particle distributions near the vascular wall. Other limitation is the lack of a detailed description capturing the individual blood particle behavior in microscopic regions near the vascular wall, including leukocyte rolling, biochemical bonding, and penetration to the wall. Nevertheless, the three-phase model does offer hemodynamic insight into how leukocytes with RBC dispersion migrate to the low WSS region, rather than to the high WSS region. In future studies, the model combined with mass transfer such as oxygen and carbon dioxide will be used to predict the effect of oxygen contributing to the progress of atherosclerotic plaque [21].

In this study, we have presented a model that describes a three-phase non-Newtonian concentrated flow of blood applied to a wide physiological range of hematocrits, including low shear rates. The CFD simulation predicted the migration and segregation of leukocytes to specific vascular sites, in particular the secondary vortex, which correlates with relatively low WSS because of the flow- and geometry-dependent interactions with RBCs in pulsatile flow. Such prediction is possible only with a three-phase flow model including RBCs. This hemodynamic study combined with medical imaging research will advance our understanding on arterial plaque progression that is able to guide therapy of the vulnerable plaque. Multiphase CFD simulations may give further insight into the hemodynamic characteristics of such vulnerable plaque and vascular remodeling in the human blood vessels under *in vivo* complex flow conditions.

Acknowledgement

This study was supported under US Department of Energy contract DE-AC02-06CH11357.

References

[1] Anderson TB, Jackson R. A fluid mechanical description of fluidized beds. I&EC Fundam 1967;6:524–39.
[2] Berthier B, Bouzerar R, Legallais C. Blood flow patterns in an anatomically realistic coronary vessel: influence of three different reconstruction methods. J Biomech 2002;35:1347–56.
[3] Brooks DE, Goodwin JW, Seaman GVF. Interactions among erythrocytes under shear. J Appl Physiol 1970;28:172–7.
[4] Burns MP, DePaola N. Flow-conditioned HUVECs support clustered leukocyte adhesion by coexpressing ICAM-1 and E-selectin. Am J Physiol Heart Circ Physiol 2005;288:H194–204.
[5] Caro CG, Fitz-Gerald JM, Schroter RC. Arterial wall shear and distribution of early atheroma in man. Nature 1969;223:1159–61.
[6] Cokelet GR, Goldsmith HL. Decreased hydrodynamic resistance in the two-phase flow of blood through small vertical tubes at low flow rates. Circ Res 1991;68:1–17.
[7] Cristini V, Kassab GS. Computer modeling of red blood cell rheology in the microcirculation: a brief overview. Ann Biomed Eng 2005;33:1724–7.
[8] DePaola N, Davies PF, Pritchard Jr WF, Florez L, Harbeck N, Polacek DC. Spatial and temporal regulation of gap junction connexin43 in vascular endothelial cells exposed to controlled disturbed flows in vitro. Proc Natl Acad Sci USA 1999;96:3154–9.
[9] Falk E, Shah PK, Fuster V. Coronary plaque disruption. Circulation 1995;92:657–71.
[10] FLUENT user's guide. Fluent Inc.; 2003.
[11] Fung YC. Biomechanics: mechanical properties of living tissues. New York: Springer; 1993.
[12] Gidaspow D. Multiphase flow and fluidization: continuum and kinetic theory descriptions. New York: Academic Press; 1994.
[13] Goldsmith HL, Spain S. Margination of leukocytes in blood flow through small tubes. Microvasc Res 1984;27:204–22.
[14] Hinds MT, Park YJ, Jones SA, Giddens DP, Alevriadou BR. Local hemodynamics affect monocytic cell adhesion to a three-dimensional flow model coated with E-selectin. J Biomech 2001;34:95–103.
[15] Hyun S, Kleinstreuer C, Archie Jr JP. Hemodynamics analyses of arterial expansions with implications to thrombosis and restenosis. Medical Eng Phys 2000;22:13–27.
[16] Iimura K, Higashitani K. Simulation of the hydrodynamic drag force on aggregates. Adv Powder Technol 2005;16:87–96.
[17] Jung J, Hassanein A. Multiphase hemodynamic analysis of cardiovascular systems. In: 2005 AIChE annual meeting. 2005.
[18] Jung J, Gidaspow D, Gamwo IK. Measurement of two kinds of granular temperatures, stresses and dispersion in bubbling beds. Ind Eng Chem Res 2005;44:1329–41.
[19] Jung J, Lyczkowski RW, Panchal CB, Hassanein A. Multiphase hemodynamic simulation with pulsatile flow in a coronary artery. J Biomech 2006;39:2064–73.
[20] Jung J, Hassanein A, Lyczkowski RW. Hemodynamic computation using multiphase flow dynamics in a right coronary artery. Ann Biomed Eng 2006;34:393–407.
[21] Karino T, Goldsmith HL. Flow Behaviour of blood cells and rigid spheres in an annular vortex. Philos Trans R Soc Lond Ser B 1977;279:413–45.
[22] Kleinstreuer C. Two-phase flow: theory and application. New York: Taylor & Francis; 2003.
[23] Longest PW, Kleinstreuer C. Comparison of blood particle deposition models for non-parallel flow domains. J Biomech 2003;36:421–30.
[24] Longest PW, Kleinstreuer C, Buchanan JR. Efficient computation of micro-particle dynamics including wall effects. Comput Fluids 2004;33:577–602.
[25] Malek AM, Alper SL, Izumo S. Hemodynamic shear stress and its role in atherosclerosis. J Am Med Assoc 1999;282:2035–42.
[26] Munn LL, Melder RJ, Jain RK. Analysis of cell flux in the parallel plate flow chamber: implications for cell capture studies. Biophys J 1994;67:889–95.
[27] Munn LL, Melder RJ, Jain RK. Role of erythrocytes in leukocyte-endothelial interactions: mathematical model and experimental validation. Biophys J 1996;71:466–78.
[28] Nobis U, Pries AR, Cokelet GR, Gaehtgens P. Radial distribution of white cells during blood flow in small tubes. Microvasc Res 1985;29:295–304.
[29] Phillips RJ, Amstrong RC, Brown RA. A constitutive equation for concentrated suspension that accounts for shear-induced particle migration. Phys Fluids A 1992;4:30–40.
[30] Pritchard WF, Davies PF, Derafshi Z, Polacek DC, Tsao R, Dull RO, et al. Effects of wall shear stress and fluid recirculation on the localization

of circulating monocytes in a three-dimensional flow model. J Biomech 1995;28:1459–69.
[31] Ross R. Atherosclerosis—an inflammatory disease. N Engl J Med 1999;340:115–26.
[32] Schoenhagen P, White RD, Nissen SE, Tuzcu EM. Coronary imaging: angiography shows the stenosis, but IVUS, CT, and MRI show the plaque. Cleve Clin J Med 2003;70:713–9.
[33] Stone PH, Coskun AU, Yeghiazarians Y, Kinlay S, Popma JJ, Kuntz RE, et al. Prediction of sites of coronary atherosclerosis progression: in vivo profiling of endothelial shear stress, lumen, and outer vessel wall characteristics to predict vascular behavior. Curr Opin Cardiol 2003;18:458–70.
[34] Sun C, Migliorini C, Munn LL. Red blood cells initiate leukocyte rolling in postcapillary expansions: a lattice Boltzmann analysis. Biophys J 2003;85:208–22.
[35] Traub O, Berk BC. Laminar shear stress: mechanisms by which endothelial cells transduce an atheroprotective force. Arterioscler Thromb Vasc Biol 1998;18:677–85.
[36] Walpola PL, Gotlieb AI, Cybulsky MI, Langille BL. Expression of ICAM-1 and VCAM-1 and monocyte adherence in arteries exposed to altered shear stress. Arterioscler Thromb Vasc Biol 1995;15: 2–10.
[37] Wentzel JJ, Janssen E, Vos J, Schuurbiers JCH, Krams R, Serruys PW, et al. Extension of increased atherosclerotic wall thickness into high shear stress regions is associated with loss of compensatory remodelling. Circulation 2003;108:17–23.
[38] Wojnarowski J. Numerical study of bileaf heart valves performance. In: International scientific practical conference: efficiency of engineering education in XX century. 2001.